





Dynamic Equilibrium Sets of the Atomic Content of Galaxies across Cosmic Time

Liang Wang¹, Danail Obreschkow¹, Claudia D. P. Lagos^{1,2}, Sarah M. Sweet³ , Deanne B. Fisher³, Karl Glazebrook³ ,
Andrea V. Macciò^{4,5}, Aaron A. Dutton⁴, and Xi Kang⁶

¹International Centre for Radio Astronomy Research (ICRAR), M468, University of Western Australia,
35 Stirling Hwy, Crawley, WA 6009, Australia; liang.wang@uwa.edu.au

²ARC Centre of Excellence for All Sky Astrophysics in 3 Dimensions (ASTRO 3D)

³Centre for Astrophysics and Supercomputing, Swinburne University of Technology, P.O. Box 218, Hawthorn, VIC 3122, Australia

⁴New York University Abu Dhabi, P.O. Box 129188, Saadiyat Island, Abu Dhabi, United Arab Emirates

⁵Max-Planck-Institut für Astronomie, Königstuhl 17, D-69117 Heidelberg, Germany

⁶Purple Mountain Observatory, the Partner Group of MPI für Astronomie, 2 West Beijing Road, Nanjing 210008, People's Republic of China

Received 2018 August 16; revised 2018 October 12; accepted 2018 October 14; published 2018 November 27

Abstract

We analyze 88 independent, high-resolution, cosmological zoomed-in simulations of disk galaxies in the NIHAO simulations suite to explore the connection between the atomic gas fraction and angular momentum (AM) of baryons throughout cosmic time. The study is motivated by the analytical model of Obreschkow et al., which predicts a relation between the atomic gas fraction f_{atm} and the integrated atomic stability parameter $q \equiv j\sigma/(GM)$, where M and j are the mass and specific AM of the galaxy (stars+cold gas) and σ is the velocity dispersion of the atomic gas. We show that the simulated galaxies follow this relation from their formation ($z \simeq 4$) to the present within ~ 0.5 dex. To explain this behavior, we explore the evolution of the local Toomre stability and find that 90%–100% of the atomic gas in all simulated galaxies is stable at any time. In other words, throughout the entire epoch of peak star formation until today, the timescale for accretion is longer than the timescale to reach equilibrium, thus resulting in a quasi-static equilibrium of atomic gas at any time. Hence, the evolution of f_{atm} depends on the complex hierarchical growth history primarily via the evolution of q . An exception is galaxies subject to strong environmental effects.

Key words: galaxies: dwarf – galaxies: evolution – galaxies: formation – galaxies: spiral – methods: numerical

1. Introduction

A comprehensive theory of galaxy evolution requires understanding the assembly and evolution of the stellar disks and spheroids of galaxies, as well as the coevolution of these components with the interstellar medium (ISM) and circumgalactic medium (CGM). The accurate modeling of these gaseous components in galaxies is challenging, as the gas is subject to nonlinear gravitational, hydrodynamic, and radiative forces. Several physical processes significantly affect the geometry and thermodynamic phase of the gas, such as cold flow accretion (Kereš et al. 2005), hot mode accretion (e.g., Rees & Ostriker 1977; White & Rees 1978; Putman et al. 2012; Werk et al. 2014), stellar winds from evolved stars (Kalirai et al. 2008; Leitner & Kravtsov 2011), and recycling of the metal-rich gas ejected through stellar winds (Oppenheimer et al. 2010; Brook et al. 2014; Übler et al. 2014). Owing to the time-dependent complex geometry of gas flows into and out of galaxies, the detailed evolution of different gas components has yet to be understood.

Neutral atomic hydrogen (HI) dominates the hydrogen budget in local galaxies, except at the highest column densities ($>10 M_{\odot} \text{pc}^{-2}$), where this gas normally transitions into the molecular (H_2) phase. HI is the critical waypoint between the ionized CGM and star formation in the disk (Leroy et al. 2008). Detailed studies of HI are therefore invaluable to understanding the formation of galaxies at large. Direct observations in 21 cm emission and absorption (Ewen & Purcell 1951) have revealed a plethora of relationships between the HI content and other galaxy properties, most notably the star formation rate (Kennicutt 1989), stellar mass (e.g., Dutton & van den Bosch 2009; Obreschkow & Rawlings 2009; Dutton et al. 2011;

Catinella et al. 2013; Maddox et al. 2015), spin (Huang et al. 2012; Obreschkow et al. 2016), and morphology (Catinella et al. 2010; Brown et al. 2015, 2017).

The atomic gas fraction is defined as

$$f_{\text{atm}} = \frac{1.35 M_{\text{HI}}}{M}, \quad (1)$$

where the total mass $M = M_{\star} + 1.35(M_{\text{HI}} + M_{\text{H}_2})$, and M_{\star} , M_{HI} , and M_{H_2} are stellar mass, HI mass, and H_2 mass, respectively. The factor of 1.35 accounts for the universal $\sim 26\%$ helium fraction at redshift $z = 0$. Computational examinations show that f_{atm} depends sensitively on the numerical resolution, subgrid physics, e.g., feedback from supernovae and active galactic nuclei, (e.g., Duffy et al. 2012; Davé et al. 2013; Stinson et al. 2015; Crain et al. 2017; Diemer et al. 2018) and physical processes related to the cosmological environment, e.g., ram pressure stripping and tidal interactions, (Cunnamea et al. 2014; Rafieferantsoa et al. 2015). It is necessary to identify the key driver(s) that set(s) f_{atm} to first order in some well-defined sense.

Several recent empirical and computational works have highlighted that the specific angular momentum (AM) of galaxies at fixed stellar mass is strongly correlated with their atomic gas fraction (e.g., Dutton et al. 2010; Huang et al. 2012; Obreschkow et al. 2015b; Lagos et al. 2017; Romeo & Mogotsi 2018; Stevens et al. 2018; Zoldan et al. 2018).

Obreschkow et al. (2016; hereafter O16) introduced a parameter-free analytical model that predicts f_{atm} as a function of mass and AM in equilibrium disks. This model assumes that galactic disks have an exponential surface density profile and are locally either fully atomic or non-atomic: the disk is atomic

where and only where the atomic gas is stable in the sense of Toomre (1964) at the characteristic dispersion velocity σ of the warm neutral medium (about 10 km s^{-1}). In this model f_{atm} only depends on the so-called integrated atomic stability parameter

$$q = \frac{j_{\text{gal}} \sigma_{\text{gas}}}{GM_{\text{gal}}}, \quad (2)$$

first introduced by Obreschkow & Glazebrook (2014), where M_{gal} and j_{gal} are the mass and specific AM of the galaxy (stellar disk+cold gas) and G is the gravitational constant. O16 predicted that f_{atm} depends on q , approximately as

$$f_{\text{atm}} = \min \{1, 2.5q^{1.12}\}, \quad (3)$$

with small (<10%) variations subject to the shape of the rotation curve.

To the extent that the assumptions of O16 remain valid across cosmic time, the evolution of f_{atm} should depend on a galaxy's complex assembly and interaction history only (or at least predominantly) via the evolution of q . This hypothesis is an interesting test case for cosmological simulations, which provide comprehensive information on the history of the atomic gas in evolving galaxies. The aim of this study is to examine the dependency between f_{atm} and q across the cosmic time in the Numerical Investigation of a Hundred Astrophysical Objects, NIHAO (Wang et al. 2015) project. The NIHAO simulations are a suite of 88 hydrodynamical cosmological zoomed-in simulations implementing the tree-smoothed particle hydrodynamics (SPH), GASOLINE2. The NIHAO runs keep the same stellar physics for the whole mass range. The stellar mass of each halo in the NIHAO sample agrees with the prediction from abundance-matching (Wang et al. 2015). The galaxies in the NIHAO sample reproduce several baryonic properties in observations, such as the star formation main sequence (Wang et al. 2015), the column density profile of cool H I (Gutcke et al. 2017), the Tully–Fisher relation (Dutton et al. 2017), and the local velocity function (Macciò et al. 2016). Therefore, NIHAO is well suited to studying the relation (if any) between f_{atm} and q through cosmic time across six orders of magnitude in stellar mass from 10^5 to $10^{11} M_{\odot}$.

This paper is structured as follows. The simulation techniques, in particular the modeling of the different hydrogen phases and computation of relevant kinematic parameters, are described in Section 2. The properties of the simulated galaxies and the key results concerning the relation between the atomic gas fraction and q parameter are presented in Section 3, along with a discussion of the physical mechanisms leading to these results. A summary and outlook are given in Section 4.

2. Simulations

This section gives an overview of the NIHAO simulations and briefly describes the subgrid physics routines, including the scheme used to separate the hydrogen into ionized (H II), atomic, and molecular phases. We also describe the methods used to compute the kinematic parameters used in our analysis.

2.1. Simulations and Subgrid Physics

In this study, we use 88 zoomed-in simulations from the NIHAO project (Wang et al. 2015). In these simulations, the particle mass of the cold dark matter (CDM) and gas particles

depends on the galaxy mass, such that each galactic halo is resolved by roughly 10^6 CDM particles at redshift $z = 0$. These zoomed-in volumes have been extracted from three different N -body CDM simulations with box sizes of 60, 20, and $15 h^{-1} \text{ Mpc}$, respectively (see Dutton & Macciò 2014 for details). All these runs used the cosmological parameters from the *Planck* satellite (Planck Collaboration et al. 2014). Dark matter particle masses range from $\sim 10^4 M_{\odot}$ in our lowest-mass halos to $\sim 10^6 M_{\odot}$ in our most massive halos, and their force-softening lengths range from ~ 150 to $\sim 900 \text{ pc}$, respectively. Gas particles are less massive by a factor of $(\Omega_{\text{dm}}/\Omega_{\text{b}}) \simeq 5.48$, where Ω_{dm} and Ω_{b} are density parameters of dark matter and baryon, and the corresponding force-softening lengths are 2.34-times smaller.

The simulated galaxies uniformly cover a range in stellar mass of $10^5 \lesssim M_{\star}/M_{\odot} \lesssim 10^{11}$ at $z = 0$. Most systems of $M_{\star} < 10^9 M_{\odot}$ are rotationally dwarfs with disky stellar and cold gas morphology, sometimes showing typical irregularities of dwarfs. Most of the more massive galaxies are spiral systems with rotating central overdensities (pseudo-bulges; Wang et al. 2018). A few most massive galaxies are early-type systems dominated by a spheroid. Two systems have undergone a major merger just before $z = 0$, and show significant merger remnant structures.

We use the SPH code GASOLINE2 (Wadsley et al. 2017). The code includes a subgrid model for turbulent mixing of metal and energy (Wadsley et al. 2008), ultraviolet (UV) heating, photoionization, and cooling due to hydrogen, helium, and metals (Shen et al. 2010).

The star formation and feedback models are those used in the Making Galaxies in a Cosmological Context simulations (Stinson et al. 2013). The gas is converted into stars according to the Kennicutt-Schmidt law when it satisfies a temperature and density threshold. Stars feed both metals and energy back in to the ISM gas surrounding the region where they formed. Supernova (SN) feedback is implemented using the blastwave formalism described in Stinson et al. (2006). Pre-SN feedback is an attempt to consider radiation energy from massive stars. Heating is introduced immediately after massive stars form based on how much starlight is radiated. Our simulations use thermal feedback to provide pressure support and increase gas temperature above the star formation threshold, and thus to decrease star formation. Full details on the star formation and feedback modeling can be found in Wang et al. (2015).

2.2. Partition of Hydrogen into H II, H I, and H₂

The partitioning of the gas particles into H II, H I, and H₂ is done following a two-stage scheme, similar to those presented by Rahmati et al. (2015), Lagos et al. (2015, 2016), Bahé et al. (2016), and Crain et al. (2017). First, for the transition from H II to neutral (H I + H₂) gas, we use the fitting function of Rahmati et al. (2013) to calculate the neutral fraction on a particle-by-particle basis from the gas temperature, gas density, and UV background modeled by Haardt & Madau (2001). This fitting function accounts for collisional ionization, photoionization by a homogeneous UV background and radiative recombination. Second, the neutral gas particles are fractionally divided into H I and H₂ using the model of Gnedin & Kravtsov (2011). This model relies on a phenomenological model for H₂ formation, approximating how H₂ forms on the surfaces of dust grains and is destroyed by the interstellar radiation field. In this model, the

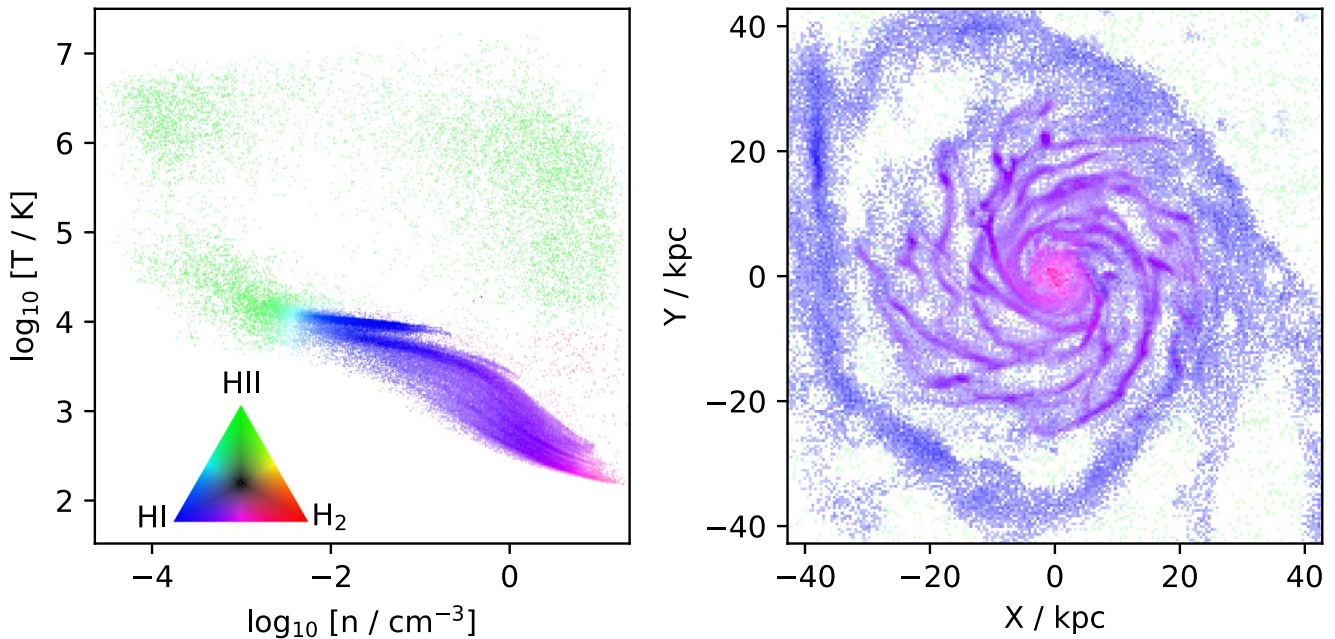


Figure 1. Temperature–density phase-diagram (left) and spatial distribution (right) of all the hydrogen in the Milky-Way-like NIHAO galaxy g8.26e11 at $z = 0$. In each pixel, the balance between the three hydrogen phases is represented by hue according to the triangle, while intensity represents the total hydrogen mass on a nonlinear scale ($\gamma = 0.5$) to show low-density regions.

H_2/HI ratio of individual gas particles depends on the dust-to-gas mass ratio, gas surface density, and UV field, which we calculated as in Lagos et al. (2015). Lagos et al. (2015) used the models of Krumholz (2013) and Gnedin & Draine (2014) to calculate the H_2 fraction for individual particles, finding similar results. Diemer et al. (2018) models the UV radiation from young stars by assuming a constant escape fraction and optically thin propagation throughout the galaxy and improves the calculation of H_2 mass. Our test cases show that the partitioning scheme in Diemer et al. (2018) provides similar HI mass as well.

The phase partitioning of hydrogen is illustrated in Figure 1 for a Milky-Way-like galaxy (NIHAO object g8.26e11) at $z = 0$, both in the temperature–density phase-space, as well as in the real space phase-on projection of the galaxy. In each pixel of the two panels, the hue represents the phase mixing and intensity represents the total hydrogen density. As expected, most H_2 is found in the dense center and spiral arms of the galaxy, whereas the HI dominates in the outskirts.

The majority of the hydrogen in this galaxy resides in the high-density ($n > 10^{-3} \text{ cm}^{-3}$) and low-temperature ($T < 10^4 \text{ K}$) region of the phase-diagram, where the material is almost exclusively neutral. This statement only applies to the region of the galaxy and does not conflict with the likely fact that most of the hydrogen in the universe resides in the ionized CGM or intergalactic medium (Crain et al. 2017).

Because of the limited resolution, the ISM gas particles around supernovae are always dense and would quickly radiate their energy away due to efficient cooling at high density. For this reason, cooling is disabled for particles inside the blast region (for a duration specified in McKee & Ostriker 1977). The locally disabled cooling artificially maintains too much ionized hydrogen in the high-density ($n > 1 \text{ cm}^{-3}$), high-temperature ($T > 10^4 \text{ K}$) state. We consider this gas to be always ionized, and thus this is of no concern for the present analysis of atomic hydrogen.

2.3. The q Parameters

This section describes the methods to compute the quantities needed to study the q - f_{atm} relation of O16. To study this relation, we must calculate the atomic gas velocity dispersion σ , galaxy mass, and AM. All these quantities are measured in the galactic region confined to a flat cylinder aligned with the galactic plane, of radius $5R_{50}$ and height $0.2R_{50}$, where R_{50} is the stellar half-mass radius of that galaxy. In principle, O16 only accounted for a disk component, hence M and j in this study should perhaps exclude bulge stars, although in the case of disk-like pseudo-bulges the choice is not straightforward. In this paper, we do not decompose galaxies into disks and bulges and simply include all stellar material in M and j . This represents at most a modest error, since our galaxies are disk-dominated or even bulge-less at lower stellar masses ($M_* < 10^{10} M_\odot$). Note that elliptical galaxies generally exhibit very low atomic gas fractions ($f_{\text{atm}} < 0.01$), negligible for the cosmic HI budget.

The neutral atomic gas fraction f_{atm} is simply calculated via Equation (1), where the HI and H_2 masses result directly from the phase splitting of Section 2.2.

The specific AM j of the galaxy is computed as

$$j = \frac{|\sum M_i \mathbf{r}_i \times \mathbf{v}_i|}{\sum M_i}, \quad (4)$$

where i goes over all baryonic particles in the cylindrical region, M_i are the particle masses (stellar+HI + H_2 , excluding HII), \mathbf{r}_i are the position vectors from the center of mass, and \mathbf{v}_i are the velocities relative to the center of the mass frame. Given j , we then evaluate q via Equation (2). Because the disk thickness can affect the stability (Romeo & Falstad 2013), it is reasonable to measure the three-dimensional dispersion to take the thickness into account. Therefore, unlike in O16, we do not assume a universal value for the atomic dispersion σ , but

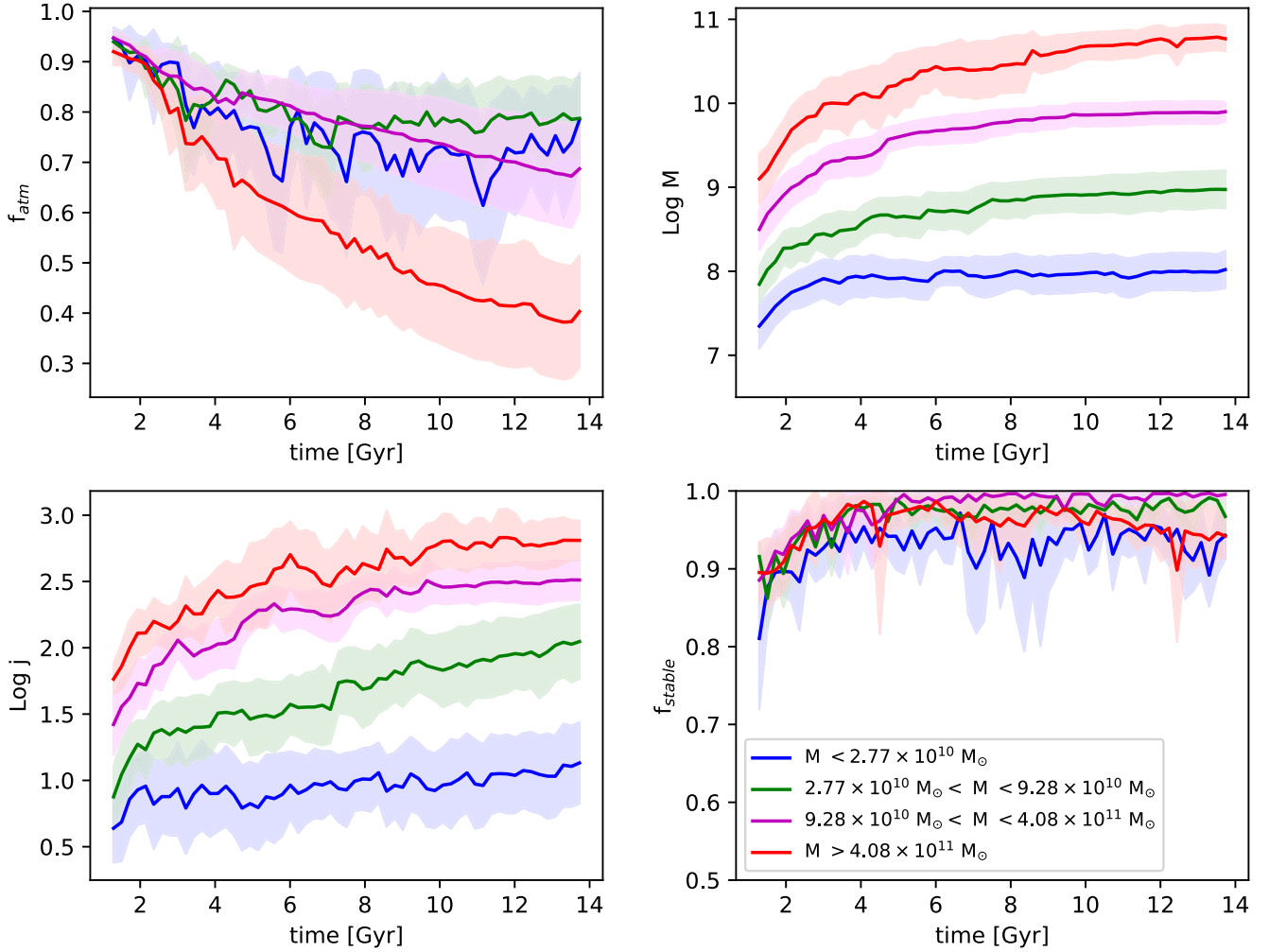


Figure 2. Average evolution of atomic gas fractions (upper left), baryon mass (upper right), specific angular momenta (lower left), and stable mass fraction (lower right) of the 88 NIHAO galaxies in four bins of virial mass at $z = 0$. The shaded regions show the 1σ standard deviations. The three lower-mass bins ($< 4.08 \times 10^{11} M_{\odot}$) show a similar evolution, with an atomic gas fraction of 70%–80% at $z = 0$. The most massive galaxies in the sample, however, have an atomic gas fraction that decreases steeply with time and become stellar-mass-dominated at $t \gtrsim 8$ Gyr. Baryonic mass and specific AM can vary strongly and systematically between different mass bins and generally increase with time. In all mass bins, the stable mass fraction lies above $\sim 90\%$ at any time shortly after the galaxies form.

instead compute this quantity across the galaxy disk from the simulation as described in the [Appendix](#).

Finally, we quantify the stable mass fraction of the atomic hydrogen. A thin disk in gravitational equilibrium is stable if and only if the so-called Toomre parameter Q (Toomre 1964) is larger than unity. For a single-component gaseous disk, this parameter takes the form $Q_{\text{gas}} = \kappa\sigma/\pi G\Sigma$, where σ and Σ are the local radial velocity dispersion and surface density of the gas, respectively, and κ is the local epicyclic frequency. A two-component (stellar+gas) stability parameter can be approximated using the formalism of Romeo & Wiegert (2011). This computation of Q and the prerequisite computations of σ and κ are detailed in the [Appendix](#). Each galaxy is sub-divided into 400 cells, that is, into 20 angular bins and 20 radial bins with approximately equal numbers of gas particles. In each cell i , the Toomre Q_i is evaluated and the stable atomic gas fraction is computed as

$$f_{\text{stable}} = M_{\text{HI}}^{-1} \sum_{i \in Q_i > 1} M_{\text{HI},i}. \quad (5)$$

Following this definition, f_{stable} is bound between 0 (all HI unstable) and 1 (all HI stable).

3. Results and Discussion

This section describes the cosmic evolution of f_{atm} of our 88 simulated galaxies, in relation to the cosmic evolution of other dynamical and kinematic parameters.

3.1. Evolution of Basic Quantities

The upper left panel of Figure 2 shows the evolution of the mean atomic gas fraction in four bins of dynamical mass at $z = 0$. We choose the bin breaks to have equal numbers of galaxies. The general trend of the atomic gas fraction for all galaxies is to decrease with cosmic time, as expected due to the build-up of stellar mass. The three lower-mass bins ($< 4.08 \times 10^{11} M_{\odot}$) show a similar evolution, with an atomic gas fraction of 70%–80% by $z = 0$. The most massive galaxies in the sample, however, have an atomic gas fraction that decreases steeply with time and becomes stellar-mass-dominated at $t \gtrsim 8$ Gyr. The coevolution of the baryonic mass and specific AM are shown in the upper right and lower left panels of Figure 2. Naturally, these quantities can vary strongly and systematically between different mass bins and generally increase with time. The evolutionary tracks of mass and AM

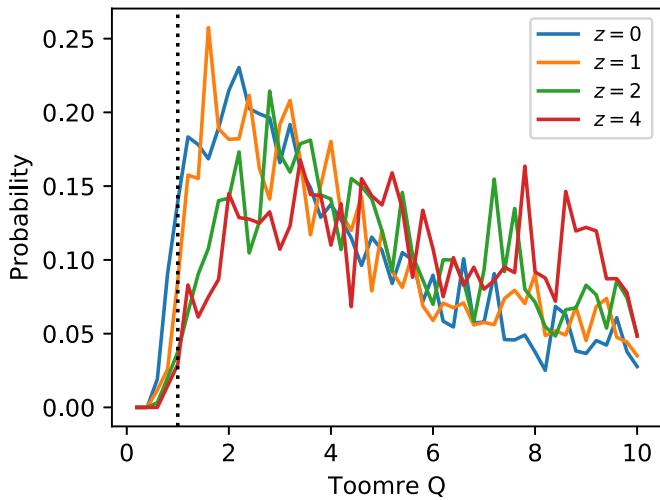


Figure 3. Mean distribution of the net two-component Toomre Q (the Appendix) for all simulated galaxies. The distribution function of Q across the galaxies highlights that most of the stable gas lies significantly above $Q = 1$ at all redshifts.

are obviously distinct between different mass bins, while those of the atomic gas fraction f_{atm} are overlapping for the three lower-mass bins. Hence, neither the mass nor the AM alone can determine the atomic gas fraction at any given cosmic time.

Following O16, we expect f_{atm} to correlate strongly with q . This expectation requires the atomic disks to be saturated in a stable equilibrium. We therefore explore the stable atomic gas fraction (Equation (5)) as a function of cosmic time in the lower right panel of Figure 2. In all mass bins this fraction lies above $\sim 90\%$ at any time shortly after the galaxies form, when the universe was roughly 1 Gyr old. Figure 3, which shows the mean distribution function of Q in all galaxies at different redshifts, highlights that most of the stable gas lies significantly above $Q = 1$.

The reason for the high cold gas stability at all times is that the characteristic timescale of cold gas accretion onto the galaxies is almost always larger than that of the feedback-regulated $\text{HI} \leftrightarrow \text{H}_2$ conversion loop in unstable regions. To illustrate this feature, we study the conversion rates in the MW and a dwarf galaxy. Figure 4 shows three mass flow rates between different gas phases in two representative NIHAO galaxies (g8.26e11 in the Milky Way mass range and g6.96e10 in the dwarf galaxy range). The individual rates of the local molarization ($\text{HI} \rightarrow \text{H}_2$) and feedback-driven dissociation ($\text{H}_2 \rightarrow \text{HI}$) are much larger than the resulting net $\text{HI} \rightarrow \text{H}_2$ conversion rate. The latter equals the cold gas accretion rate ($\text{HII} \rightarrow \text{HI}$) onto the disk in the steady state situation, which roughly applies to our galaxies. In other words, the HI phase is in a quasi-static equilibrium at almost any time in the NIHAO galaxies.

This situation is also expected in real galaxies, as long as the timescale of the local $\text{HI} \rightarrow \text{H}_2$ conversion (i.e., without accounting for feedback) is shorter than the timescale of cold gas accretion onto the disk. We expect this to be the case in most spiral systems, where the local $\text{HI} \rightarrow \text{H}_2$ conversion (before feedback) is similar to the local freefall time, of the order of $\sim 1\text{--}10$ Myr (Krumholz 2014). However, this argument breaks down in very low-density and low-metallicity systems, where the H_2 formation time can increase significantly (Krumholz 2013), and hence the instantaneous self-regulation assumed in the O16 model, breaks down. However, such

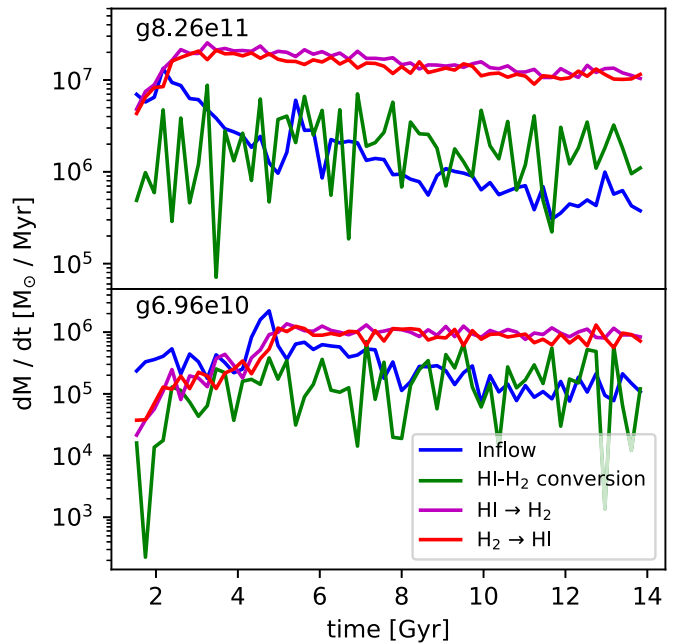


Figure 4. Neutral hydrogen accretion rate (blue), HI-H₂ conversion rate (green), and mass flow rates from HI to H₂ (magenta) and vice versa (red) in two representative NIHAO galaxies (g8.26e11 in the Milky Way mass range and g6.96e10 in the dwarf galaxy range). The individual rates of the local molarization ($\text{HI} \rightarrow \text{H}_2$) and feedback-driven dissociation ($\text{H}_2 \rightarrow \text{HI}$) are much larger than the resulting net $\text{HI} \rightarrow \text{H}_2$ conversion rate. The HI phase is in a quasi-static equilibrium at almost any time in the NIHAO galaxies.

galaxies are typically dwarf galaxies (high q values), where this model predicts purely atomic disks anyways.

Incidentally, as discussed by Stinson et al. (2015), the HI mass in disk NIHAO galaxies remains approximately constant from $z = 1$ to $z = 0$. This means that at $z = 1$ the quasi-static equilibrium reaches a state where the HI accretion matches its depletion. In the present context this can be understood as a leveling-off in the evolution of j/M , which implies that newly accreted HI will settle onto the existing HI disk and hence reduce its stability until the same amount of HI is converted into molecules.

In conclusion, the finding that most HI is dynamically stable at any time, irrespective of the galaxy mass, motivates the analysis of f_{atm} in the framework of O16.

3.2. Evolution of a Single System in q - f_{atm} Space

Let us first consider the case of the single Milky-Way-like galaxy (NIHAO object g8.26e11) already used in Figure 1. We remind the reader that this galaxy is representative of the Milky-Way-like galaxies in NIHAO, both in mass and morphology. Figure 5 shows the morphological evolution of this galaxy at four redshifts. The morphology at redshift $z = 4$ is compact and irregular, due to the turbulent initial collapse of low-AM material. At $z = 2$, this galaxy starts developing a disk, which becomes steadily more extended and dusty.

The evolutionary track of this galaxy in q - f_{atm} space (see Figure 6) appears to scatter around the stability relation (dashed line). The galaxy starts somewhat above the relation, due to the fast accretion of HI, which has not yet settled in a stable equilibrium disk. From there, f_{atm} first decreases dramatically due to disk heating by minor mergers (an effect discussed in detail by Stevens et al. 2018 in the context of semi-analytic

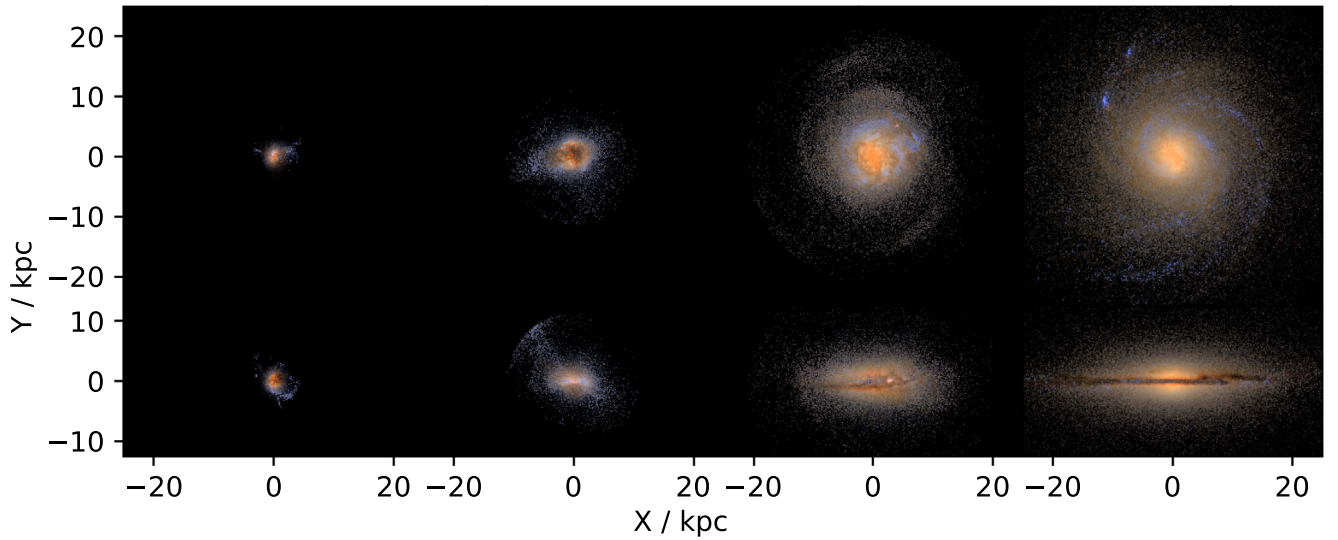


Figure 5. Face-on (upper panel) and edge-on (lower panel) views of g8.26e11 at redshift $z = 4, 2, 1, 0$ (left to right). The image is produced by post-processing through the Monte Carlo radiative transfer code SUNRISE.

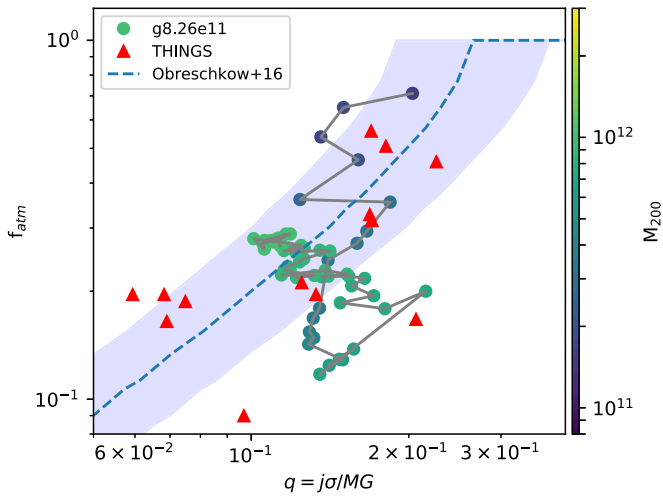


Figure 6. Evolutionary track of the Milky-Way-like NIHAO galaxy g8.26e11 in q - f_{atm} space from redshift $z = 4$ to $z = 0$ (connected round dots). The dots are color-coded by dynamical mass. The red triangles show the local spiral galaxies from the THINGS survey analyzed by O16 and the dashed line is Equation (3) of their model. The evolutionary track of this galaxy in q - f_{atm} space appears to evolve around the relation of O16 roughly within its empirical scatter.

models), making the galaxy HI-deficient relative to the amount of HI that could be dynamically supported. The galaxy evolves with low f_{atm} (0.2 dex lower than the predicted relation) for ~ 1 Gyr. Then, the galaxy gradually accumulates new HI, which mostly settles in a stable disk, moving this object steadily back onto the stability relation. The upper panel of Figure 4 shows that the neutral gas accretion of this galaxy decreases monotonously before redshift $z \sim 2$, and keeps constant at the late stage. The decreasing efficiency of neutral gas accretion at early times couples with the decrease in f_{atm} .

3.3. Statistical Relation between f_{atm} and q

The location of all 88 NIHAO galaxies in the q - f_{atm} space is shown in Figure 7 at four different redshifts. The dashed line shows the prediction of the equilibrium model. The simulations

exhibit a redshift evolution of f_{atm} at fixed q parameter since redshift $z \sim 4$. The maximum deviations of simulated galaxies relative to the model of O16 are contained within $\lesssim 0.5$ dex, despite the six orders of magnitude in stellar mass spanned by this sample. The NIHAO simulations therefore confirm that the atomic gas fraction is connected to the cosmic evolution of q . There are nonetheless clear systematic deviations between the analytical model and the simulations, which we will discuss now.

First, at $z = 4$, all simulated galaxies exhibit very high atomic gas fractions, even at the lowest q values, where lower gas fractions are expected from the stability model. This is because the timescale for accretion is indeed shorter than that of the H I-H₂ transition in these few galaxies. Hence, the analytical equilibrium model is bound to fail (see Section 3.1).

Second, at q values larger than $q = 1/(\sqrt{2}e)$, where the O16 model predicts purely atomic disks ($f_{\text{atm}} = 1$), the simulated galaxies fall systematically below the model. This discrepancy increases from $z = 4$, where $f_{\text{atm}} \approx 0.9$ in this regime, to $z = 0$, where $f_{\text{atm}} \approx 0.6$ – 0.7 . Most galaxies in this range of q are dwarf galaxies. In the simulation (as well as in reality) such galaxies often show irregular morphologies that defy the assumption of an axially symmetric disk and show more local instabilities than expected in such a simple model. This is one reason for the offset between the model and the simulations. However, it should be emphasized that observations of dwarf galaxies at $q > 1/(\sqrt{2}e)$ at $z = 0$ normally exhibit atomic gas fractions that indeed lie around 0.8–0.9 (Obreschkow et al. 2016). It is therefore possible that our result somewhat underpredicts the atomic gas in dwarf galaxies. In either case, the reason for the better agreement with the O16 relation at $z = 4$ is that, at such high redshifts, almost all galaxies have barely started to form stars.

Third, the stable mass fraction does not correlate with the deviation between the simulated galaxy and the model of O16. Most galaxies with an unstable gaseous disk lie at q values larger than $q = 1/(\sqrt{2}e)$, and the fraction of such galaxies in the sample is less than 5%. By inspecting the evolution of these unstable systems snapshot-by-snapshot, we found that all the most unstable systems ($f_{\text{stable}} < 0.5$) are only unstable for one snapshot. In other words, the timescale of the instability is

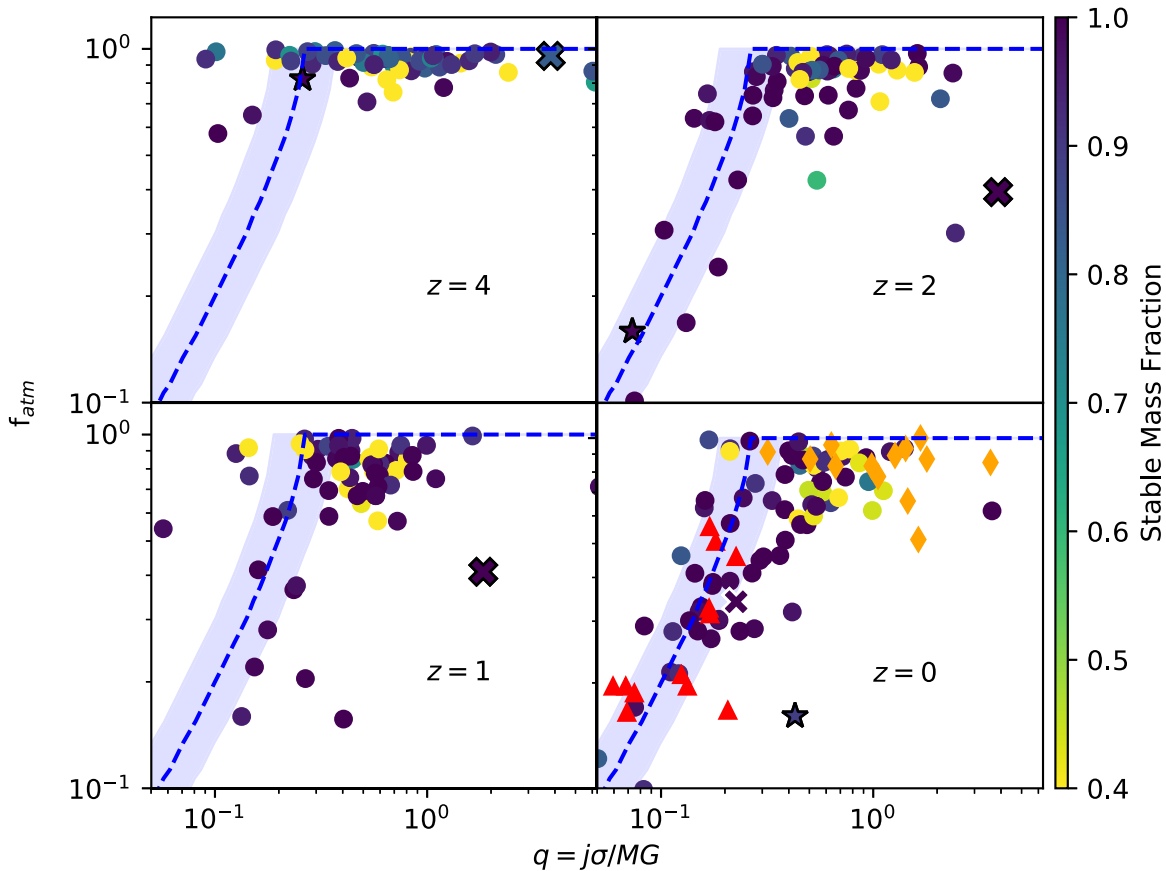


Figure 7. Evolution of atomic gas fraction vs. q parameter. The blue dashed line shows the O16 relation given in Equation (3) with a 40% uncertainty (in f_{atm}) as the HI dispersion exhibits an intrinsic empirical scatter (Obreschkow et al. 2016). All points are color-coded by the stable mass fraction of the galaxies at the given redshift. The red triangles and orange diamonds show the local spiral galaxies from the THINGS survey and the LITTLE THINGS survey analyzed by O16. The simulated galaxies are broadly consistent with the prediction of the model of O16 and therefore confirm that the atomic gas fraction is connected to the cosmic evolution of q . Two outliers with irregular morphologies discussed in Section 3.3 are marked as \star symbol (g8.13e11) and \times symbol (g1.37e11).

shorter than the temporal resolution of the NIHAO simulation. We are therefore currently unable to determine how long exactly the unstable phases lasts.

Finally, two interesting outliers are marked as different symbols in Figure 7. A one-by-one inspection of these galaxies shows that they have irregular morphologies. The NIHAO object g8.13e11 (\star symbol) at redshift $z = 0$ has a polar ring at $z = 0$. Object g1.37e11 (\times symbol) shows a clear signature of a recent merger event at $z = 2$ and acquires a spherical morphology with faint streams at redshift $z = 1$.

4. Conclusions

In this paper, we used the NIHAO galaxy simulation suite (Wang et al. 2015) to analyze the dependency between the atomic gas fraction f_{atm} and the integrated atomic stability parameter q (Obreschkow et al. 2016) across cosmic time. The q parameter was defined by O16 and used to develop an analytical equilibrium model to predict the atomic gas fraction in disks. NIHAO is a large set of high-resolution, cosmological, zoomed-in hydrodynamical galaxy formation simulations in the mass range between dwarf galaxies to Milky-Way-mass galaxies. The simulated galaxies have a realistic cosmological environment and realistic dynamical and kinematic properties, making them ideal to test the O16 model in a full cosmological setup. Our results are as follows:

1. The atomic gas fractions for all galaxies start at unity and decrease monotonically as the galaxies evolve. The galaxies in the most massive mass bin consume their gas rapidly, while galaxies in lower-mass bins decrease more mildly.
2. Most ($\gtrsim 90\%$) atomic gas of most galaxies is stable at any cosmic time. Most of the stable gas is clearly stable (Toomre $Q > 2$).
3. The NIHAO sample is qualitatively consistent with the model of O16, which predicts the atomic gas fraction to depend on mass and AM only via the *integrated atomic stability parameter* q . The simulation and model agree at almost any time.

The last point is the most important finding. It implies that gravitational equilibrium is the dominant factor regulating f_{atm} at any particular time. The deeper reason for this simple conclusion is that the timescale of HI accretion is almost always longer than that of the local HI \leftrightarrow H₂ feedback loop. An exception to this rule is galaxies undergoing strong interactions, which can lead to massive instantaneous accretion and/or remove large amounts of HI via, for instance, starbursts, dynamical heating, or stripping or fueling of a central black hole. Some of these additional processes have recently been explored by Stevens et al. (2018) in a semi-analytic context, but a full physics treatment of these processes remains to be presented.

We thank Joop Schaye and Alessandro Romeo for useful feedback on this manuscript. We also thank the anonymous referee for a constructive report that helped improve the clarity of this paper. The analysis was performed using the pynbody package (<http://pynbody.github.io>), which was written by Andrew Pontzen and Rok Roškar in addition to the authors. C.L. has received funding from a Discovery Early Career Researcher Award (DE150100618) and by the ARC Centre of Excellence for All Sky Astrophysics in 3 Dimensions (ASTRO 3D), through project number CE170100013. This research was carried out on the High Performance Computing resources at New York University Abu Dhabi; on the THEO cluster of the Max-Planck-Institut für Astronomie; and on the HYDRA clusters at the Rechenzentrum in Garching.

Appendix Calculation of the Stability Parameter of Galaxies in NIHAO

In order to measure the stability parameter that was shown in Section 2, we sample the simulated galaxy with 400 cells across a plane perpendicular to its spin. In each cell, we measure the surface density Σ , local radial velocity dispersion σ , and local epicyclic frequency κ .

Gas and stellar mass surface densities were calculated from the enclosed mass within the cell as $\Sigma_{\text{gas}} = M_{\text{gas}}/S$ and $\Sigma_{\text{star}} = M_{\text{star}}/S$, where M_{gas} and M_{star} are total gaseous and stellar mass within each cell and S is the area of each cell.

We calculate the star-forming gas velocity dispersion of galaxies by considering the velocity difference with the center of mass, and calculating the component of this velocity that is parallel to the rotation axis:

$$\sigma_{\text{gas}} = \sqrt{\frac{\sum_i m_i (v_{z,i}^2 + \sigma_p^2)}{\sum m_i}}. \quad (6)$$

Here, i are all gas particles within each cell, m_i is the mass of particle i , and $v_{z,i}$ is the vertical velocity of the i particle with respect to the center of mass. The velocity dispersion contribution from the gas pressure of gas particles is σ_p and is defined as

$$\sigma_p = \sqrt{\frac{P}{\rho}}, \quad (7)$$

where P and ρ are the gas pressure and density. In the case of stars, we calculate the velocity dispersion in a similar manner, but in the case of stars there is no thermal pressure, so the stellar velocity dispersion is simply

$$\sigma_{\text{star}} = \sqrt{\frac{\sum_i m_i v_{z,i}^2}{\sum m_i}}. \quad (8)$$

As simulations have full kinematic information of particles, we can measure the epicyclic frequency by definition

$$\kappa = \Omega + \omega, \quad (9)$$

where Ω is the z -component of angular velocity of the cell relative to the center of galaxy, and ω is the z -component of angular velocity of all particles within the cell relative to their mass center. The angular velocity can be calculated by $\omega = J_z/I_{zz}$, where J_z is the AM of all particles within the cell

and I_{zz} is the zz -component of the inertia tensor

$$I_{zz} = \sum_{k=1}^N m_k (x_k^2 + y_k^2). \quad (10)$$

To measure the Toomre (1964) parameter for each cell, we use the properties above as:

$$Q_{\text{gas}} = \frac{\kappa \sigma_{\text{gas}}}{\pi G \Sigma_{\text{gas}}}, \quad (11)$$

$$Q_{\text{star}} = \frac{\kappa \sigma_{\text{star}}}{\pi G \Sigma_{\text{star}}}. \quad (12)$$

We combine Q_{gas} and Q_{star} to get a net Toomre parameter following Romeo & Wiegert (2011):

$$\frac{1}{Q_{\text{net}}} = \begin{cases} \frac{W}{Q_{\text{star}}} + \frac{1}{Q_{\text{gas}}}, & Q_{\text{star}} \geq Q_{\text{gas}} \\ \frac{W}{Q_{\text{gas}}} + \frac{1}{Q_{\text{star}}}, & Q_{\text{gas}} \geq Q_{\text{star}} \end{cases} \quad (13)$$

where

$$W = \frac{2\sigma_{\text{gas}}\sigma_{\text{star}}}{\sigma_{\text{gas}}^2 + \sigma_{\text{star}}^2}. \quad (14)$$

ORCID iDs

Sarah M. Sweet  <https://orcid.org/0000-0002-1576-2505>
Karl Glazebrook  <https://orcid.org/0000-0002-3254-9044>

References

- Bahé, Y. M., Crain, R. A., Kauffmann, G., et al. 2016, *MNRAS*, 456, 1115
 Brook, C. B., Stinson, G., Gibson, B. K., et al. 2014, *MNRAS*, 443, 3809
 Brown, T., Catinella, B., Cortese, L., et al. 2015, *MNRAS*, 452, 2479
 Brown, T., Catinella, B., Cortese, L., et al. 2017, *MNRAS*, 466, 1275
 Catinella, B., Schiminovich, D., Cortese, L., et al. 2013, *MNRAS*, 436, 34
 Catinella, B., Schiminovich, D., Kauffmann, G., et al. 2010, *MNRAS*, 403, 683
 Crain, R. A., Bahé, Y. M., Lagos, C. D. P., et al. 2017, *MNRAS*, 464, 4204
 Cunnama, D., Andrianomena, S., Cress, C. M., et al. 2014, *MNRAS*, 438, 2530
 Davé, R., Katz, N., Oppenheimer, B. D., Kollmeier, J. A., & Weinberg, D. H. 2013, *MNRAS*, 434, 2645
 Diemer, B., Stevens, A. R. H., Forbes, J. C., et al. 2018, *ApJS*, 238, 33
 Duffy, A. R., Meyer, M. J., Staveley-Smith, L., et al. 2012, *MNRAS*, 426, 3385
 Dutton, A. A., Conroy, C., van den Bosch, F. C., et al. 2011, *MNRAS*, 416, 322
 Dutton, A. A., & Macciò, A. V. 2014, *MNRAS*, 441, 3359
 Dutton, A. A., Obreja, A., Wang, L., et al. 2017, *MNRAS*, 467, 493
 Dutton, A. A., & van den Bosch, F. C. 2009, *MNRAS*, 396, 141
 Dutton, A. A., van den Bosch, F. C., & Dekel, A. 2010, *MNRAS*, 405, 1690
 Ewen, H. I., & Purcell, E. M. 1951, *Natur*, 168, 356
 Gnedin, N. Y., & Draine, B. T. 2014, *ApJ*, 795, 37
 Gnedin, N. Y., & Kravtsov, A. V. 2011, *ApJ*, 728, 88
 Gutcke, T. A., Stinson, G. S., Macciò, A. V., et al. 2017, *MNRAS*, 464, 2796
 Haardt, F., & Madau, P. 2001, in *Clusters of Galaxies and the High Redshift Universe Observed in X-rays*, ed. D. M. Neumann & J. T. T. Van (Savoie: CEA0), 64
 Huang, S., Haynes, M. P., Giovanelli, R., & Brinchmann, J. 2012, *ApJ*, 756, 113
 Kalirai, J. S., Hansen, B. M. S., Kelson, D. D., et al. 2008, *ApJ*, 676, 594
 Kennicutt, R. C., Jr. 1989, *ApJ*, 344, 685
 Kereš, D., Katz, N., Weinberg, D. H., & Davé, R. 2005, *MNRAS*, 363, 2
 Krumholz, M. R. 2013, *MNRAS*, 436, 2747
 Krumholz, M. R. 2014, *PhR*, 539, 49
 Lagos, C. d. P., Crain, R. A., Schaye, J., et al. 2015, *MNRAS*, 452, 3815
 Lagos, C. d. P., Theuns, T., Schaye, J., et al. 2016, *MNRAS*, 459, 2632
 Lagos, C. d. P., Theuns, T., Stevens, A. R. H., et al. 2017, *MNRAS*, 464, 3850
 Leitner, S. N., & Kravtsov, A. V. 2011, *ApJ*, 734, 48
 Leroy, A. K., Walter, F., Brinks, E., et al. 2008, *AJ*, 136, 2782

- Macciò, A. V., Udrescu, S. M., Dutton, A. A., et al. 2016, *MNRAS*, **463**, L69
- Maddox, N., Hess, K. M., Obreschkow, D., Jarvis, M. J., & Blyth, S.-L. 2015, *MNRAS*, **447**, 1610
- McKee, C. F., & Ostriker, J. P. 1977, *ApJ*, **218**, 148
- Obreschkow, D., & Glazebrook, K. 2014, *ApJ*, **784**, 26
- Obreschkow, D., Glazebrook, K., Bassett, R., et al. 2015a, *ApJ*, **815**, 97
- Obreschkow, D., Glazebrook, K., Kilborn, V., & Lutz, K. 2016, *ApJ*, **824L**, 26
- Obreschkow, D., Meyer, M., Popping, A., et al. 2015b, in *Advancing Astrophysics with the Square Kilometre Array (AASKA14)* (Giardini Naxos, Italy), 138
- Obreschkow, D., & Rawlings, S. 2009, *MNRAS*, **394**, 1857
- Oppenheimer, B. D., Davé, R., Kereš, D., et al. 2010, *MNRAS*, **406**, 2325
- Planck Collaboration, Ade, P. A. R., Aghanim, N., et al. 2014, *A&A*, **571**, AA16
- Putman, M. E., Peek, J. E. G., & Joung, M. R. 2012, *ARA&A*, **50**, 491
- Rafieferantsoa, M., Davé, R., Anglés-Alcázar, D., et al. 2015, *MNRAS*, **453**, 3980
- Rahmati, A., Pawlik, A. H., Raičević, M., & Schaye, J. 2013, *MNRAS*, **430**, 2427
- Rahmati, A., Schaye, J., Bower, R. G., et al. 2015, *MNRAS*, **452**, 2034
- Rees, M. J., & Ostriker, J. P. 1977, *MNRAS*, **179**, 541
- Romeo, A. B., & Falstad, N. 2013, *MNRAS*, **433**, 1389
- Romeo, A. B., & Mogotsi, K. M. 2018, *MNRAS*, **480**, L23
- Romeo, A. B., & Wiegert, J. 2011, *MNRAS*, **416**, 1191
- Shen, S., Wadsley, J., & Stinson, G. 2010, *MNRAS*, **407**, 1581
- Stevens, A. R. H., Lagos, C. D. P., Obreschkow, D., & Sinha, M. 2018, *MNRAS*, **481**, 5543
- Stinson, G. S., Brook, C., Macciò, A. V., et al. 2013, *MNRAS*, **428**, 129
- Stinson, G. S., Dutton, A. A., Wang, L., et al. 2015, *MNRAS*, **454**, 1105
- Stinson, G. S., Seth, A., Katz, N., et al. 2006, *MNRAS*, **373**, 1074
- Toomre, A. 1964, *ApJ*, **139**, 1217
- Übler, H., Naab, T., Oser, L., et al. 2014, *MNRAS*, **443**, 2092
- Wadsley, J. W., Keller, B. W., & Quinn, T. R. 2017, *MNRAS*, **471**, 2357
- Wadsley, J. W., Veeravalli, G., & Couchman, H. M. P. 2008, *MNRAS*, **387**, 427
- Wang, L., Dutton, A. A., Stinson, G. S., et al. 2015, *MNRAS*, **454**, 83
- Wang, L., Obreschkow, D., del P. Lagos, C., et al. 2018, *MNRAS*, in press (arXiv:1811.02239)
- Werk, J. K., Prochaska, J. X., Tumlinson, J., et al. 2014, *ApJ*, **792**, 8
- White, S. D. M., & Rees, M. J. 1978, *MNRAS*, **183**, 341
- Zoldan, A., De Lucia, G., Xie, L., Fontanot, F., & Hirschmann, M. 2018, *MNRAS*, **481**, 1376